Research Article

Showkat Ahmad Lone, F. M. Allehiany, Sadia Anwar, Sana Shahab, Anwar Saeed*, and Sayed M. Eldin*

Investigating effects of Lorentz forces and convective heating on ternary hybrid nanofluid flow over a curved surface using homotopy analysis method

https://doi.org/10.1515/ntrev-2023-0125 received May 16, 2023; accepted September 5, 2023

Abstract: This work investigates the ternary hybrid nanofluid flow over an extending curved surface. The surface is impermeable and convective with hot working fluid water. Additionally, TiO₂, CoFe₂O₄, and MgO nanoparticles are suspended with water to form a tri-hybrid nanofluid. The modeled equations are presented in the partial differential equation form and are then converted to ordinary differential equations with appropriate similarity variables. The semi-analytical solution is determined by homotopy analysis method. The impacts of magnetic field, Joule heating, chemical reaction, Brownian motion, and thermophoresis on flow profiles, Nusselt number, and Sherwood number are determined using tables and figures. The findings of this study demonstrated that as the magnetic parameter upsurges, the velocity distribution shrinkages, while the temperature distribution escalates. The greater curvature factor boots the velocity, thermal, and volumetric fraction distribution. The thermal and volumetric fraction distributions are the increasing functions of thermophoresis factor. The higher magnetic factor, Eckert number, and thermal Biot number increase the Nusselt number, while they reduce the higher Brownian and thermophoretic factors. The higher thermophoresis and Brownian motion factors heighten the Sherwood number. Furthermore, it has been noted that using nanofluid (TiO₂-water) and hybrid nanoliquid (TiO₂-CoFe₂O₄/water), the transfer of energy rate increases by up to 17.31 and 31.72% as the nanoparticle parameter increases from 0.01 to 0.04, respectively. However, the energy transference rate in case of ternary hybrid nanoliquid (TiO₂-MgO-CoFe₂O₄/water) is 47.972%.

Keywords: nanofluid, hybrid nanofluid, ternary hybrid nanofluid, convective heat transfer, Joule heating, chemical reaction, curved surface

curvilinear coordinates (m)

titanium dioxide

Nomenclature

(r, s)

 TiO_2

^{*} Corresponding author: Anwar Saeed, Department of Mathematics, Abdul Wali Khan University, Mardan, 23200, Khyber Pakhtunkhwa, Pakistan, e-mail: anwarsaeed769@gmail.com

^{*} Corresponding author: Sayed M. Eldin, Center of Research, Faculty of Engineering, Future University in Egypt New Cairo, New Cairo, Egypt, e-mail: sayed.eldin22@fue.edu.eg

Showkat Ahmad Lone: Department of Basic Sciences, College of Science and Theoretical Studies, Saudi Electronic University, (Jeddah-M), Riyadh 11673, Saudi Arabia

F. M. Allehiany: Mathematics Department, Faculty of Sciences, Umm Al-Qura University, Mecca, Saudi Arabia

Sadia Anwar: Department of Mathematics, College of Arts and Sciences, Wadi Ad Dawasir (11991), Prince Sattam Bin Abdulaziz University, Al-Kharj, Saudi Arabia

Sana Shahab: Department of Business Administration, College of Business Administration, Princess Nourah Bint Abdulrahman University, P.O. Box 84428, Riyadh 11671, Saudi Arabia

positive fixed number b T_f surface temperature (K) specific heat capacity (J K⁻¹ kg⁻¹) C_p electrical conductivity (S m⁻¹) Rc curvature factor Ec Eckert number chemical reaction factor γ Nb Brownian motion factor $f'(\eta)$ velocity field MgO magnesium oxide $u_w = bs$ stretching velocity (m s⁻¹) $CoFe_2O_4$ cobalt ferrite density (kg m⁻³) ρ surface volumetric fraction distribution (mol m^{-3})

k	thermal diffusivity (W K ⁻¹ m ⁻¹)
M	magnetic factor
Bi	thermal Biot number
Q	heat source parameter
Sc	Schmidt number
Nt	thermophoresis factor

1 Introduction

Titanium dioxide (TiO₂) is an inorganic substance that is used extensively as a white pigment. Compared with many other inorganic pigments, TiO₂ has the advantages such as high stability, being non-toxic, and low cost. TiO₂ has three polymorphs: anatase, rutile, and brookite, but only anatase and rutile crystal forms are used as pigments. Both anatase and rutile crystals have very high refractive indices, and their particles can scatter visible light almost completely. In the early application of TiO₂ as pigment, it was found that paint faded more rapidly than others when painted films were exposed to the Sun and ultraviolet light. Coating with inorganic compounds such as alumina or silica suppressed the catalytic activity on the surface and improved the weather resistance. Hence, titanium dioxide is used in a wide range of applications such as white pigment.

Modifications of metal oxide nanoparticles with metallic element are the ideal choice for heterogeneous photocatalysis to eliminate different kinds of contamination from wastewater. Among the metal and metal oxide nanoparticles, MgO nanoparticles played a significant role in antimicrobial activity, dye degradation, and phenol degradation activity. Ag nanoparticles are, without a doubt, the most widely used inorganic nanoparticles with huge applications. MgO nanoparticles acquired additional consideration due to their vast applications in medical, catalysis, as absorbents, *etc.*

The reason for cobalt spinel ferrites (CoFe₂O₄) gaining so much attention is because of their excellent chemical and good mechanical stabilities at room temperature, their moderate saturation magnetization, high coercivity, and their strong anisotropy. The chemical and mechanical stabilities of cobalt spinel ferrites are very different from their bulk counterparts. Due to all of these properties, cobalt ferrites have been broadly used in biotechnology, catalysis, biomedical, magnetic drug delivery, solar cells, magnetic cards, recording devices, and sensors. CoFe₂O₄ nanoparticles should have high magnetization values and narrow-size distribution for catalysis applications.

Nanofluid flow refers to the movement of a fluid that contains suspended tiny particles with diameters typically fluctuating from 1 to 100 nm. The flow behavior of nanofluids

is different from that of pure fluids, as the nanoparticles can affect the viscosity, thermal flow, and flow characteristics of the fluid. Nanofluids have been extensively used recently due to their potential applications in areas such as energy storage, electronic cooling, and biomedical engineering. The idea of such fluids was floated first by Choi and Eastman [1] to augment the thermal behavior of normal fluids. The flow behavior of nanofluids is influenced by numerous factors, comprising the size and shape of nanoparticles, the volumetric fraction distribution and type of the nanoparticles, the flow rate and temperature of the fluid, and the geometry of the system. Mourad et al. [2] executed a numerical analysis of the entropy production and magnetohydrodynamics (MHD) natural convection of a Cu-water nanofluid that was enclosed within a wavy cylinder and heated Koch snowflake. Acharya et al. [3] deliberated on nanofluid flow on a gyratory disk using the influences of nanolayer and diameter of nanoparticles and determined that temperature has increased for progression in nanolayer ratio as well as thermal radiation but has declined with upsurge in diameter of nanoparticles. Shahid et al. [4] conducted numerical experiment for bioconvective nanofluid flow on a porous sheet. Bhatti et al. [5] scrutinized MHD Williamson nanofluid flow through a spinning circular sheet with influence of microorganisms and proved that the liquid velocity has weakened with progression in nanoparticles' volumetric fraction distribution and magnetic factor, while, on the other side, the thermal distribution has augmented. Wijayanta [6,7] reported on the thermal evaluation of natural convection in an opening using the numerical approach to estimate the laminar natural convective flow along with heat exchange in triangle-shaped cavities. Makarim et al. [8] investigated numerically the Marangoni convection that occurs when steam is absorbed into a water-soluble lithium bromide solution. Kumar et al. [9] investigated theoretically the mathematical model of nanoliquid flow past a sheet with the impact of magnetic factor and chemically reactive effects.

Hybrid nanofluid flow is fluid flow that contains a mixture of two or more dissimilar nature of nanoparticles, such as metal oxide and carbon-based nanoparticles. The combination of nanoparticles can lead to synergistic effects, where the resulting nanofluid has enhanced thermal and/or mechanical properties compared to a single-component nanofluid. The flow behavior of hybrid nanofluids can be more complex than that of single-component nanofluids, as the different types of nanoparticles can interact with each other and with the base fluid in various ways. The properties of hybrid nanofluids can be influenced by factors such as the nature of the particles, particle—fluid interactions, and the flow conditions. The aim of investigating hybrid nanofluid is to gain a better idea about the flow behavior and properties of hybrid nanofluids, as well as to develop

methods for optimizing their performance in various applications such as thermal management in electronic devices and energy storage systems. Zhang et al. [10] discussed hybrid nanofluid flow on a surface using nickel and tantalum nanoparticles using the effects of magnetic field and have concluded that flow has propagated faster in case of tantalum nanoparticles and Darcy number, while it has declined with progression in magnetic effects. Khan et al. [11] inspected bioconvective nanofluid flow with impact of binary chemical reactions, viscous dissipation, and activated energy on a heated needle. Chu et al. [12] examined MHD hybrid nanofluid flow through a channel using the impact of nanoparticles' shape. Ojjela [13] discussed numerically the thermal transportation for silica-alumina hybrid nanofluid flow using modeling simulation. Gumber et al. [14] discussed the thermal flow for hybrid nanofluid flow on a surface using impacts of suction as well as injection and thermal radiations. Slimani et al. [15] discussed the MHD hybrid nanofluid's flow with heat distribution in a trimmed cone with open domains that were stimulated by a magnetic flux. The study reveals that the rate of Nusselt number enhances with an upshot of magnetic flux.

Ternary hybrid nanofluid flow states the movement of a fluid that contains three different types of nanoparticles suspended in it. As discussed earlier, nanofluids are made by dispersing tiny particles, typically less than 100 nm in size, into a pure fluid. These particles are often metallic, ceramic, or carbon-based, and they can considerably alter the thermal and rheological properties of the fluid. A ternary hybrid nanofluid flow would contain three different types of nanoparticles, which could potentially lead to unique properties such as improved thermal conductivity or enhanced heat transfer characteristics. Arif et al. [16] analyzed the heat transmission of fractal model for ternary hybrid nanofluid flow in a conduit using different shapes of nanoparticles. Shahzad et al. [17] inspected the influences of pressure variation on ternary hybrid nanofluid flow through a circular conduit. When three unlike forms of nanoparticles are dispersed into a base fluid, they can considerably alter the heat and rheological characteristics of liquid, leading to unique behavior. Sudharani et al. [18] assessed computationally the ternary hybrid nanofluid flow affected by linearly radiated effects and slip flow and have deduced that the thermal flow performance has amplified more in case of ternary hybrid nanoparticles in comparison with other two fluids. The study of ternary hybrid nanofluid flow involves both computational modeling and experimental studies to better understand the behavior and potential applications of these complex fluids. Guedri et al. [19] inspected the thermally radiative flow of ternary hybrid nanofluid on a nonlinearly elongating surface using the Darcy-Forchheimer model.

Convective heat transfer refers to the transfer of heat through fluid and solid surface, typically a gas or a liquid that is in motion. The heat is transferred due to the movement of the fluid, which carries thermal energy away from the surface and transports it to another location. Convective heat transfer is an important mechanism in different phenomena, like cooling of electronic devices, the transfer of heat in a car's radiator, and the circulation of air in a room. The analysis and prediction of convective heat transfer is an important area of study in many fields, including engineering, physics, and materials science. Shevchuk [20] inspected convective heat transportation for geometry of disk and cone by using the advanced asymptotic expansion method and turning effects of the cone on flow model. Olayemi et al. [21] inspected the parametric convective thermal transportation for fluid flow on a cylinder placed in a square conduit and deduced that the rate of heat transmission has been observed to rise with increasing aspect ratio and Rayleigh number. Manna et al. [22] discussed MHD fluid flow and production of entropy on a circular surface subject to the impact of convective thermal transportation. Wang and Wang [23] simulated computationally the convective heat transportation through a packed bed and have proved that the fluid flow and thermal transportation are affected by the porosity factor. Shi et al. [24] discussed the convective thermal transportation properties for fluid flow on a cylinder through a confined space.

Joule heating is a phenomenon in which electrical energy is changed to thermal energy. This heat is generated as a consequence of the collisions among the electrons and the atoms or molecules in the material. Abbas et al. [25] inspected the Darcy-Forchheimer phenomenon for fluid flow on a porous sheet subject to the impacts of Joule heating. Naseem et al. [26] deliberated the effects of Joule heating on MHD fluid flow using variable temperature and deduced that thermal transportation has amplified with progression in the Eckert number and weakened with upsurge in the Prandtl number. Rahseed et al. [27] treated analytically the MHD fluid flow with impact of Joule heating, viscous variable forces, and chemically reactive effects and have deduced that velocity distribution weakened, while thermal panels have expanded with growth in magnetic factor. Mahdy et al. [28] inspected numerically the effects of convective thermal conditions and Joule heating on a stretched sheet and have solved their modeled equations effectively using HPM. Wagas et al. [29] discussed bioconvective MHD fluid flow on a radiating stretchable sheet using viscously dissipative and Joule heating effects. Mahanthesh et al. [30] examined the production of entropy radiative thermal transportation for fluid flow in a channel subject to Joule heating and nonlinear mixed convection

effects. Gangadhar *et al.* [31] deliberated on MHD bioconvective fluid flow with influences of microorganisms and Joule heating.

Curved surfaces are used in many fields, including engineering, architecture, art, and design. They can provide strength and stability to structures, as well as aesthetic applications. In addition, curved surfaces can be used to optimize airflow, improve acoustics, and reduce drag in vehicles and aircrafts. There are many different types of curved surfaces, each with their own properties and applications. Examples include spheres, cylinders, cones, tori (donut-shaped surfaces), and more complex shapes such as hyperboloids and ellipsoids. Curved surfaces are common in everyday life and can be found in a variety of objects, including the human body, cars, airplanes, and buildings. They can be used for both aesthetic and functional purposes. For example, the curved surface of a car's body can improve its aerodynamics and reduce drag, while the curved surface of a building can improve its structural stability and provide an interesting architectural design. Mishra and Upreti [32] conducted a comparative analysis for two different types of hybrid nanoparticles on a curved sheet using the Buongiorno model and have proved that mass transportation has augmented with progression in thermophoretic and chemically reactive factors. Maity and Kundu [33] examined chemically reactive and magnetically driven flow nanofluid on a curved surface with effects of radiation and have noted that growth in mass and temperature and Biot numbers have supported, respectively, the transportation of volumetric fraction distribution and temperature. Khan et al. [34] investigated the gold nanoparticle carrier for blood flow on a curved sheet using thermal radiation, suction, and MHD effects. Sun et al. [35] investigated experimentally the control flow on a curved surface of jet at Mach 5 hypersonic flow of fluid. Fuzhang et al. [36] discussed the timebased nanofluid flow on an exponentially elongating curved surface using chemically reactive effects.

Keeping in mind the aforementioned literature, the authors decided to present the homotopic solution of the ternary hybrid nanofluid flow on an extending curved surface. The curved surface is considered to be impermeable and convectively heat with a hot working fluid. Three different types of nanoparticles (TiO₂, CoFe₂O₄, and MgO) are mixed with water (base fluid) to form ternary nanofluid. The purpose of this investigation is to answer the following research questions:

- What are the impacts of the embedded factors on velocity, temperature, and volumetric fraction distribution profiles of the ternary hybrid nanofluid flow?
- How were the flow profiles (*i.e.*, velocity, temperature, and volumetric fraction distribution profiles) if we

- increase the radius of curvature parameter of the curved surface?
- How do the skin friction, local Nusselt number, and Sherwood number behave for the increasing embedded factors?

Thus to answer these questions, we have presented this study in the following sections. Section 2 depicts the leading equations. Similarity variables are used for the transformation of partial differential equations into ordinary differential equations (ODEs). The application of the homotopy analysis method (HAM) technique for solving transformed ODEs is discussed in Section 3. The convergence of the HAM method is presented in Section 4. The results obtained using HAM, along with figures and a table, are showcased in Section 5. Finally, the conclusive outcomes are summarized in Section 6.

2 Problem statement

We have assumed the ternary hybrid nanofluid flow encompassing TiO_2 , $CoFe_2O_4$, and MgO nanoparticles over a curved sheet. The curved surface has curvilinear coordinates (r, s). The direction of the flow is denoted by s, while r represents the direction perpendicular to the flow. The stretching velocity of sheet is represented by $u_w = bs$, where b is the positive fixed number. The magnetic field B_0 is used along r-direction. For the convectively heat surface with a hot

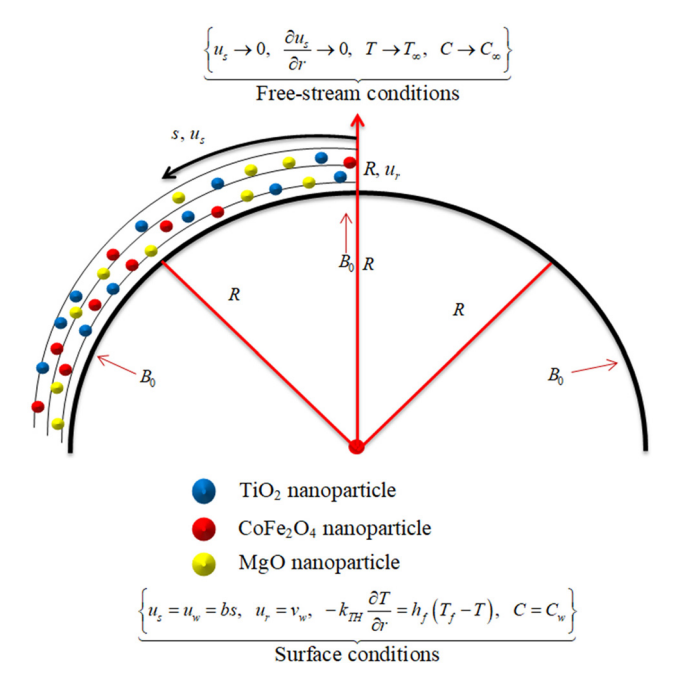


Figure 1: Curved surface representation.

fluid and temperature T_f such that $T_f > T_w$, where T_w is the surface temperature and T_∞ is its ambient value, the corresponding values for volumetric fraction distribution are C_w and C_∞ . Figure 1 shows the geometrical explanation of problem. Additionally, the following suppositions have made as:

- 1) The flow is affected by magnetic, Joule heating, and chemical reaction effects.
- 2) The surface is assumed to be impermeable.
- 3) The temperature and volumetric fraction distribution equations account for the effects of Brownian motion and thermophoresis.

Based on the aforementioned assumptions, the model equations can be expressed as follows [37-39]:

$$\frac{\partial((r+R)u_r)}{\partial r} + R\frac{\partial u_s}{\partial s} = 0,$$
(1)

$$\frac{u_s^2}{r+R} = \frac{1}{\rho_{TH}} \frac{\partial p}{\partial r},\tag{2}$$

$$u_r \frac{\partial u_s}{\partial r} + \frac{R}{r+R} u_s \frac{\partial u_s}{\partial s} + \frac{u_s u_r}{r+R} = -\frac{1}{\rho_{TH}} \frac{R}{r+R} \frac{\partial p}{\partial s} + \frac{\mu_{TH}}{\rho_{TH}} \left(\frac{\partial^2 u_s}{\partial r^2} + \frac{1}{r+R} \frac{\partial u_s}{\partial r} - \frac{u_s}{(r+R)^2} \right) - \frac{\sigma_{TH} B_0^2}{\rho_{TH}} u_s, \tag{3}$$

$$u_{r}\frac{\partial T}{\partial r} + \frac{R}{r+R}u_{s}\frac{\partial T}{\partial s} = \frac{k_{TH}}{(\rho C_{p})_{TH}} \left(\frac{\partial^{2} T}{\partial r^{2}} + \frac{1}{r+R}\frac{\partial T}{\partial r}\right) + \frac{\sigma_{TH}}{(\rho C_{p})_{TH}} B_{0}^{2}u_{s}^{2} + \frac{Q_{0}}{(\rho C_{p})_{TH}} (T - T_{\infty}) + \frac{(\rho C_{p})_{p}}{(\rho C_{p})_{TH}} \left[D_{B}\frac{\partial C}{\partial r}\frac{\partial T}{\partial r} + \frac{D_{T}}{T_{\infty}} \left(\frac{\partial T}{\partial r}\right)^{2}\right],$$

$$(4)$$

$$u_r \frac{\partial C}{\partial r} + \frac{R}{r+R} u_s \frac{\partial C}{\partial s} = D_B \left[\frac{\partial^2 C}{\partial r^2} + \frac{1}{r+R} \frac{\partial C}{\partial r} \right] + \frac{D_T}{T_\infty} \left(\frac{\partial^2 T}{\partial r^2} + \frac{1}{r+R} \frac{\partial T}{\partial r} \right) - K_r (C - C_\infty). \tag{5}$$

The constraints at boundaries are as follows [40,41]:

$$\begin{cases} u_{s} = u_{w} = bs, & u_{r} = 0, \quad -k_{TH} \frac{\partial T}{\partial r} = h_{f}(T_{f} - T), \quad C = C_{w} \text{ at } r = 0 \\ u_{s} \to 0, & \frac{\partial u_{s}}{\partial r} \to 0, \quad T \to T_{\infty}, \quad C \to C_{\infty} \text{ as } r \to \infty \end{cases}$$
 (6)

The thermophysical properties of the ternary hybrid nanofluids are characterized as follows [19,42,43]:

$$\frac{\mu_{\text{TH}}}{\mu_{f}} = \frac{1}{(1 - \chi_{1})^{2.5}(1 - \chi_{2})^{2.5}(1 - \chi_{3})^{2.5}},$$

$$\frac{\rho_{\text{TH}}}{\rho_{f}} = \frac{(1 - \chi_{1})\left[(1 - \chi_{2})\left[(1 - \chi_{3}) + \chi_{3}\frac{\rho_{s_{3}}}{\rho_{f}}\right] + \chi_{2}\frac{\rho_{s_{2}}}{\rho_{f}}\right] + \chi_{1}\frac{\rho_{s_{1}}}{\rho_{f}}}{\rho_{f}},$$

$$\frac{(\rho C_{p})_{\text{TH}}}{(\rho C_{p})_{f}} = \frac{(1 - \chi_{1})\left[(1 - \chi_{2})\left[(1 - \chi_{3}) + \chi_{3}\frac{(\rho C_{p})_{s_{3}}}{(\rho C_{p})_{f}}\right] + \chi_{2}\frac{(\rho C_{p})_{s_{2}}}{(\rho C_{p})_{f}}\right] + \chi_{1}\frac{(\rho C_{p})_{s_{1}}}{(\rho C_{p})_{f}}},$$

$$\frac{k_{\text{NF}}}{k_{f}} = \frac{k_{s_{1}} + 2k_{f} - 2\chi_{1}(k_{f} - k_{s_{1}})}{k_{s_{1}} + 2k_{f} + \chi_{1}(k_{f} - k_{s_{1}})}, \frac{k_{\text{HF}}}{k_{\text{NF}}} = \frac{k_{s_{2}} + 2k_{f} - 2\chi_{2}(k_{f} - k_{s_{2}})}{k_{s_{2}} + 2k_{f} + \chi_{2}(k_{f} - k_{s_{2}})},$$

$$\frac{k_{\text{TH}}}{k_{\text{HF}}} = \frac{k_{s_{3}} + 2k_{f} - 2\chi_{1}(\sigma_{f} - \sigma_{s_{1}})}{k_{s_{3}} + 2k_{f} + \chi_{3}(k_{f} - k_{s_{3}})}, \frac{\sigma_{\text{HF}}}{\sigma_{\text{NF}}} = \frac{\sigma_{s_{2}} + 2\sigma_{f} - 2\chi_{2}(\sigma_{f} - \sigma_{s_{2}})}{\sigma_{s_{2}} + 2\sigma_{f} + \chi_{1}(\sigma_{f} - \sigma_{s_{1}})}, \frac{\sigma_{\text{HF}}}{\sigma_{\text{NF}}} = \frac{\sigma_{s_{2}} + 2\sigma_{f} - 2\chi_{2}(\sigma_{f} - \sigma_{s_{2}})}{\sigma_{s_{2}} + 2\sigma_{f} + \chi_{2}(\sigma_{f} - \sigma_{s_{2}})},$$

$$\frac{\sigma_{\text{TH}}}{\sigma_{\text{HF}}} = \frac{\sigma_{s_{3}} + 2\sigma_{f} - 2\chi_{3}(\sigma_{f} - \sigma_{s_{3}})}{\sigma_{s_{3}} + 2\sigma_{f} + \chi_{3}(\sigma_{f} - \sigma_{s_{3}})}$$

In the aforementioned properties, χ_1 , χ_2 , and χ_3 represent the TiO₂, CoFe₂O₄, and MgO nanoparticle volume fractions, S_1 denotes the TiO₂ nanoparticle, S_2 represents the CoFe₂O₄ nanoparticle, and S_3 denotes the MgO nanoparticle. The thermophysical characteristics of nanoparticles and water are presented in Table 1.

To transform the aforementioned equations, the similarity variables are defined as follows [40,46-48]:

$$\begin{cases} \eta = r\sqrt{\frac{b}{\nu_f}}, \ u_s = bsf'(\eta), \ u_r = -\frac{R}{r+R}\sqrt{b\nu_f}f(\eta), \\ p = \rho_f(bs)^2 P(\eta), \ \theta(\eta) = \frac{T-T_\infty}{T_f-T_\infty}, \ \varphi(\eta) = \frac{C-C_\infty}{C_f-C_\infty} \end{cases}$$
(8)

Using the aforementioned similarity variables, equation (1) becomes apparent, and equation (2) can be simplified as follows:

$$\frac{\rho_f}{\rho_{TH}}P'(\eta) = \frac{1}{\eta + Rc}f'^2(\eta). \tag{9}$$

Eq. (3) can be reduced as:

$$\frac{\rho_f}{\rho_{TH}} \left(\frac{2Rc}{\eta + Rc} \right) P(\eta) = \begin{cases}
\frac{\mu_{TH}/\mu_f}{\rho_{TH}/\rho_f} \left[f'''(\eta) + \left(\frac{1}{\eta + Rc} \right) f''(\eta) - \left(\frac{1}{(\eta + Rc)^2} \right) f'(\eta) \right] \\
- \left(\frac{Rc}{\eta + Rc} \right) f'^2(\eta) - \frac{\sigma_{TH}/\sigma_f}{\rho_{TH}/\rho_f} M f'(\eta) \\
+ \left(\frac{Rc}{\eta + Rc} \right) f''(\eta) f(\eta) + \left(\frac{Rc}{(\eta + Rc)^2} \right) f'(\eta) f(\eta)
\end{cases} (10)$$

After differentiating equation (10) with respect to η and subsequently substituting it into equation (9), we obtain the following:

$$\left(\frac{\mu_{TH}/\mu_{f}}{\rho_{TH}/\rho_{f}}\right)\left[f^{i\nu}(\eta) + \left(\frac{2}{(\eta + Rc)}\right)f'''(\eta) - \left(\frac{1}{(\eta + Rc)^{2}}\right)f''(\eta) + \left(\frac{1}{(\eta + Rc)^{3}}\right)f'(\eta)\right] - \frac{\sigma_{TH}/\sigma_{f}}{\rho_{TH}/\rho_{f}}M\left[f''(\eta) + \left(\frac{1}{(\eta + Rc)}\right)f''(\eta)\right] + \left(\frac{Rc}{(\eta + Rc)^{3}}\right)\left[f'''(\eta)f(\eta) - f''(\eta)f'(\eta)\right] + \left(\frac{Rc}{(\eta + Rc)^{3}}\right)\left[f''(\eta)f(\eta) - f'^{2}(\eta)\right] - \left(\frac{Rc}{(\eta + Rc)^{3}}\right)f'(\eta)f(\eta) = 0.$$
(11)

Likewise, the remaining equations are transformed as:

$$\frac{1}{\Pr} \frac{k_{TH}/k_f}{(\rho C_p)_{TH}/(\rho C_p)_f} \left[\theta''(\eta) + \left(\frac{1}{(\eta + \text{Rc})} \right) \theta'(\xi) \right] + \left(\frac{\text{Rc}}{(\eta + \text{Rc})} \right) \theta'(\eta) f(\eta) + \text{Nt}\theta'^2(\eta)
+ \text{Nb}\phi'(\eta)\theta'(\eta) + \frac{\sigma_{TH}/\sigma_f}{(\rho C_p)_{TH}/(\rho C_p)_f} M \text{Ec}f'^2(\eta) + \frac{1}{(\rho C_p)_{TH}/(\rho C_p)_f} Q\theta(\eta) = 0.$$
(12)

$$\phi''(\eta) + \left(\frac{1}{(\eta + Rc)}\right)\phi'(\eta) + \left(\frac{Nt}{Nb(\eta + Rc)}\right)\theta'(\eta) + \left(\frac{\eta Sc}{(\eta + Rc)}\right)\phi'(\eta)f(\eta) + \frac{Nt}{Nb}\theta''(\eta) - Scy\phi(\eta) = 0.$$
 (13)

$$\begin{cases} f'(0) = 1, \ f(0) = 0, \ \theta'(0) = \frac{\text{Bi}}{k_{TH}/k_f} (\theta(0) - 1), \ \phi(0) = 1, \\ f'(\infty) \to 0, \ f''(\infty) \to 0, \ \theta(\infty) \to 0, \ \phi(\infty) \to 0. \end{cases}$$
(14)

Pressure can be reduced as:

$$P(\eta) = \left(\frac{\eta + \text{Rc}}{2\text{Rc}}\right) \begin{bmatrix} \frac{\mu_{TH}}{\mu_f} \left[f'''(\eta) + \left(\frac{1}{\eta + \text{Rc}}\right)f''(\eta) - \left(\frac{1}{(\eta + \text{Rc})^2}\right)f'(\eta)\right] - \frac{\sigma_{TH}}{\sigma_f} Mf'(\eta) + \frac{\rho_{TH}}{\sigma_f} \left[\frac{\text{Rc}}{\eta + \text{Rc}}\right]f''(\eta)f(\eta) + \frac{\rho_{TH}}{\rho_f} \left(\frac{\text{Rc}}{(\eta + \text{Rc})^2}\right)f'(\eta)f(\eta) - \frac{\rho_{TH}}{\rho_f} \left(\frac{\text{Rc}}{\eta + \text{Rc}}\right)f'^2(\eta) \end{bmatrix},$$
(15)

where $\operatorname{Rc}\left(=\sqrt{\frac{b}{v_f}}R\right)$ is the curvature factor, $M\left(=\frac{\sigma_f B_0^2}{\rho_f b}\right)$ is the magnetic parameter, $\operatorname{Bi}\left(=\frac{h_f}{k_f}\sqrt{\frac{v_f}{b}}\right)$ is the thermal Biot number, $\operatorname{Ec}\left(=\frac{b^2 s^2}{(C_p)_f (T_f - T_\infty)}\right)$ is the Eckert number, $Q\left(=\frac{Q_0}{b(\rho C_p)_f}\right)$ is the heat source parameter, $\operatorname{Pole}\left(=\frac{K_r}{b}\right)$ is the chemical reaction factor, $\operatorname{Nb}\left(=\frac{(C_f - C_\infty)D_B(\rho C_p)_{np}}{v_f(\rho C_p)_f}\right)$ is the Brownian motion factor, $\operatorname{Nt}\left(=\frac{D_T(T_f - T_\infty)(\rho C_p)_p}{v_f T_\infty(\rho C_p)_f}\right)$ is the thermophoresis factor, $\operatorname{Sc}\left(=\frac{v_f}{D_B}\right)$ is the Schmidt number, and $\operatorname{Pr}\left(=\frac{(\rho C_p)_f v_f}{k_f}\right)$ is the Prandtl number.

The quantities of interest are defined as follows:

$$\begin{cases} C_f = \frac{\tau_{rs}}{\rho_f s^2 b^2}, & \text{where } \tau_{rs} = \mu_{TH} \left(\frac{\partial u}{\partial r} - \frac{u}{r+R} \right) \Big|_{r=0}, \\ \text{Nu}_s = \frac{sq_w}{k_f (T_f - T_\infty)}, & \text{where } q_w = -k_{TH} \frac{\partial T}{\partial r} \Big|_{r=0}, \\ \text{Sh}_s = -\frac{sq_m}{D_B (C_f - C_\infty)}, & \text{where } q_m = -D_B \frac{\partial C}{\partial r} \Big|_{r=0}. \end{cases}$$

$$(16)$$

Using the similarity variables, the reduced form of equation (16) can be written as:

$$\left\{ \sqrt{Re_s} \, C_{fs} = \frac{\mu_{TH}}{\mu_f} \left\{ f''(0) - \frac{1}{Rc} f'(0) \right\}, \\
\frac{Nu_s}{\sqrt{Re_s}} = -\frac{k_{TH}}{k_f} \theta'(0), \text{ Sh} = \frac{Sh_s}{\sqrt{Re_s}} = -\phi'(0), \right\}$$
(17)

where $Re_s = \frac{bs^2}{v_F}$ is the local Reynolds number.

3 HAM solution

To apply HAM, we introduced the initial guesses and linear operators as follows:

$$f_0(\eta) = 1 - \exp(-\eta), \ \theta_0(\eta) = \frac{\text{Bi}}{(k_{TH}/k_f) + \text{Bi}} \exp(-\eta),$$

$$\phi_0(\eta) = \exp(-\eta),$$
(18)

$$L_f(\eta) = f''' - f', \ L_{\theta}(\eta) = \theta'' - \theta, \ L_{\phi}(\eta) = \phi'' - \phi,$$
 (19)

with properties:

$$L_{f}(x_{1} + x_{2}\eta + x_{3} \exp(-\eta) + x_{4} \exp(\eta)) = 0,$$

$$L_{\theta}(x_{5} \exp(-\eta) + x_{6} \exp(\eta)) = 0,$$

$$L_{\phi}(x_{7} \exp(-\eta) + x_{8} \exp(\eta)) = 0,$$
(20)

where $x_1 - x_8$ are the constants of general solution.

Table 1: Experimental values of H₂O and nanoparticles [44,45]

Properties	ρ	C_p	k	σ
H ₂ O	997.1	4,179	0.613	0.05
TiO_2	4,250	686.2	8.9538	2.38×10^{6}
$CoFe_2O_4$	4,907	700	3.7	5.51 × 10 ⁹
MgO	45	955	45	1.42×10^{-3}

3.1 Advantages of HAM

HAM has several advantages over many traditional analytical methods. It is a series expansion method that does not directly depend on small or large physical parameters. Thus, it is applicable not only for weakly but also strongly nonlinear problems. HAM is a unified method for the Lyapunov artificial small parameter method, Delta expansion method, Adomian decomposition method, and homotopy perturbation method. It gives excellent flexibility to the expression of the solution and how the solution is explicitly obtained, and it provides great freedom in choosing the base functions of the desired solution and the corresponding auxiliary linear operator of homotopy. HAM provides a simple way to ensure the convergence of the solution series and is able to combine with other techniques used in nonlinear differential equations such as spectral methods and Padé approximants.

4 Validation

To confirm the validation of the coded problem in Mathematica 12.0 software, Tables 2 and 3 are shown. The validation is confirmed under some special conditions when K varies and $\chi_1 = \chi_2 = \chi_3 = M = 0.0$. Table 2 shows the skin friction $(-\sqrt{\mathrm{Re}_s}\,C_{f\!s})$ against different values of K. Upon comparing the present findings with the published results, it can be observed that the current results exhibit a high degree of similarity to the published results. Also, Table 3 displays

the comparison of our results for $-\theta(0)$ with established results for variations in Pr, while other parameters are taken as Nb = Nt = $Q = M = \text{Ec} = \chi_1 = \chi_2 = \chi_3 = 0$, $\beta \to \infty$, and Rc $\to \infty$. In this table, the problem is converted to a flat sheet by taking the assumption when Rc $\to \infty$. In the flat surface problem, the current results and also close to the published results of the previously published works.

5 HAM convergence

The homotopic series solution contains the auxiliary factor \hbar . This parameter has the ability to control and adjust the series solution convergence. At 19th order of approximations, as given in Figure 2, the suitable range of velocity, temperature, and volumetric fraction distribution profiles have been obtained. From this figure, we can see that the velocity profile has the convergence area $-1.0 \le \hbar_f \le 1.2$, temperature profile has the convergence area $-1.0 \le \hbar_\theta \le 0.9$, and the convergence area of the volumetric fraction distribution profile is $-1.0 \le \hbar_\theta \le 0.9$.

6 Discussion of results

Next, the variations in different profiles (such as $f'(\eta)$, $\theta(\eta)$, and $\phi(\eta)$), heat transfer rate $\left(\frac{\mathrm{Nu_s}}{\sqrt{\mathrm{Re_s}}}\right)$, and mass transfer rate $\left(\frac{\mathrm{Sh_s}}{\sqrt{\mathrm{Re_s}}}\right)$ via embedded factors are discussed. Therefore, we have displayed Figures 3–11 and Tables 4 and 5 in this regard. The default values for the embedded factors are selected as Rc = 5.0, Ec = 0.5, M = 1.0, Bi = 0.5, Pr = 6.0, Q = 0.2, Y = 0.1, X_1 = X_2 = X_3 = 0.04, Nt = 0.1, Nb = 0.1, and Sc = 1.0. Figure 3(a) and (b) shows the impression of

 $Q=0.2, \ \ \gamma=0.1, \ \ \chi_1=\chi_2=\chi_3=0.04, \ \ \mathrm{Nt}=0.1, \ \ \mathrm{Nb}=0.1,$ and Sc = 1.0. Figure 3(a) and (b) shows the impression of $\chi_1=\chi_2=\chi_3$ on velocity $(f'(\eta))$ and temperature $(\theta(\eta))$ distributions, respectively. From both the figures, we see that the higher $\chi_1=\chi_2=\chi_3$ reduces $f'(\eta)$ while increasing $\theta(\eta)$. The reason is that the higher values of $\chi_1=\chi_2=\chi_3$ increase

Table 2: Comparing the values of $-\sqrt{\text{Re}_{\text{s}}} C_{\text{fs}}$ for variations in K and $\chi_1 = \chi_2 = \chi_3 = M = 0.0$

Rc	5	10	20	30	40	50	100	200	1000
Present outcomes	1.157565	1.072534	1.035464	1.023463	1.017346	1.013995	1.006963	1.003501	1.000798
Roşca and Pop [49]	1.15076	1.07172	1.03501	1.02315	1.01729	1.01380	1.00687	1.00342	1.00068
Afridi et al. [50]	1.1576312	1.0734886	1.0356098	1.0235310	1.0175866	1.0140492	1.0070384	1.0035641	1.0007993
Abbas <i>et al.</i> [51]	1.15763	1.07349	1.03561	1.02353	1.01759	1.01405	1.00704	1.00356	1.00079
Ahmad <i>et al.</i> [52]	1.157630	1.073490	_	1.023530	_	1.014050	_	1.003560	
	1.000790								
Dey <i>et al.</i> [53]	1.157630	1.073490	_	1.0223	_	_	_	_	_

Pr	0.01	0.72	1.0	2.0	7.0	10
Present outcomes	0.015664	0.463144	0.581976	0.911361	1.895420	2.308034
Khan and Pop [54]	_	_	_	0.9114	1.8954	_
Wang [55]	_	_	_	0.9114	1.8954	_
Gorla and Sidawi [56]	_	_	_	0.9114	1.8905	_
Devi and Devi [57]	_	_	_	0.91135	1.89540	_
Grubka and Bobba [58]	0.0099	0.4631	0.5820	_	_	2.3080
Gowda <i>et al.</i> [59]	0.00978	0.46273	0.58193	_	_	2.30793

Table 3: Comparison of the values of $-\theta(0)$ for different estimations of Pr, when Nb = Nt = $Q = M = \text{Ec} = \chi_1 = \chi_2 = \chi_3 = 0$ and Rc $\rightarrow \infty$

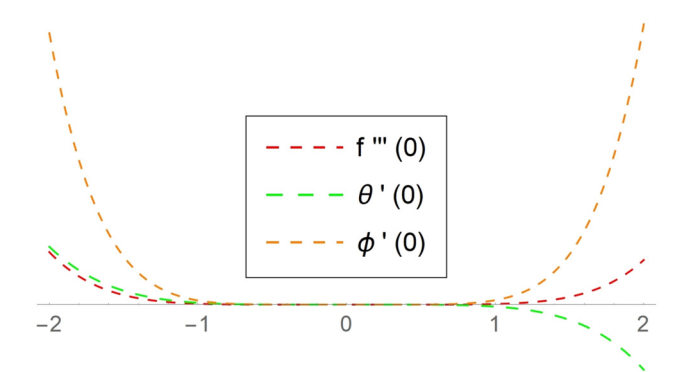


Figure 2: \hbar curves for f'''(0), $\theta'(0)$ and $\phi'(0)$.

the density of the ternary hybrid nanofluid flow due to which the fluid becomes denser, and thus, the momentum boundary layer thickness and velocity profile reduce. On the other hand, the higher values of $\chi_1 = \chi_2 = \chi_3$ increase the thermal conductivity of the ternary hybrid nanofluid flow, which, as a result, increases the thermal boundary layer thickness and temperature profile. The effects of magnetic factor (M) on velocity $(f'(\eta))$ and temperature $(\theta(\eta))$ distributions are revealed in Figure 4(a) and (b). The velocity distribution reduces, while the thermal panels upsurge with growth in M. The greater M produces the

Lorentz force that counteracts the flow of nanoparticles, and hence, the movement of nanoparticles reduces. Therefore, the greater M declines the velocity distribution. On the other hand, the opposite effect of M on temperature distribution is observed. This effect is for reducing the movement of nanoparticles because the greater Lorentz force opposes the flow motion, which results in a growth in $\theta(\eta)$ so upsurge in M boosts the temperature distribution. The effects of curvature factor (Rc) on $f'(\eta)$, $\theta(\eta)$, and $\phi(\eta)$ are displayed in Figure 5(a)–(c). The greater Rc increases $f'(\eta)$, $\theta(\eta)$, and $\phi(\eta)$. In fact, "Rc" represents the radius of the curved surface. As we increase Rc, the curved surface transforms to become flat. So by this fact, as $Rc \rightarrow \infty$ (say Rc = 1,000), the surface is not curved anymore. It is a fact that the velocity, temperature, and volumetric fraction distributions are higher on the flat surface compared to those on the curved surface. Thus, increasing Rc increases the panels $f'(\eta)$, $\theta(\eta)$, and $\phi(\eta)$. The effect of heat source (Q) on $\theta(\eta)$ is portrayed in Figure 6 with a booting behavior in $\theta(\eta)$. Actually, the increasing heat source means that we have provided extra heat to the nanofluid flow, which ultimately increases the internal heat of fluid flow. This internal temperature heightens the temperature at the boundary and so are the panels $\theta(\eta)$. Therefore, the higher Q augments $\theta(\eta)$. Figure 7(a) and (b) shows the effects of thermophoresis factor Nt on $\theta(\eta)$ and $\phi(\eta)$. These

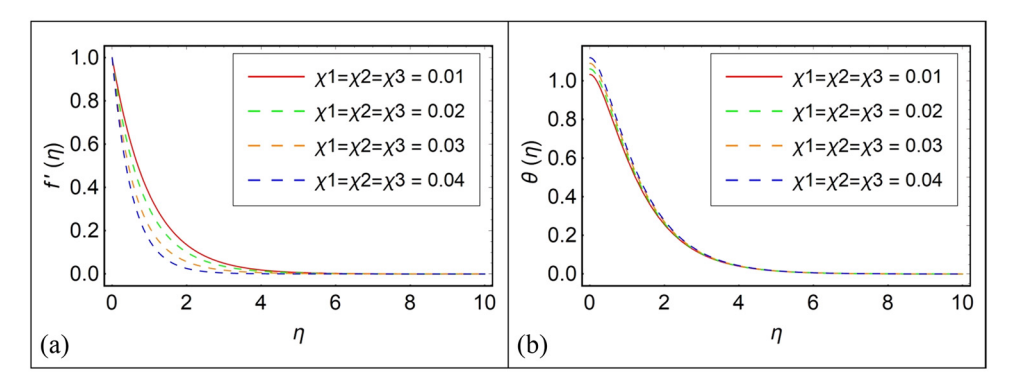


Figure 3: (a) Impression of $\chi_1 = \chi_2 = \chi_3$ on $f'(\eta)$ and (b) impression of $\chi_1 = \chi_2 = \chi_3$ on $\theta(\eta)$.

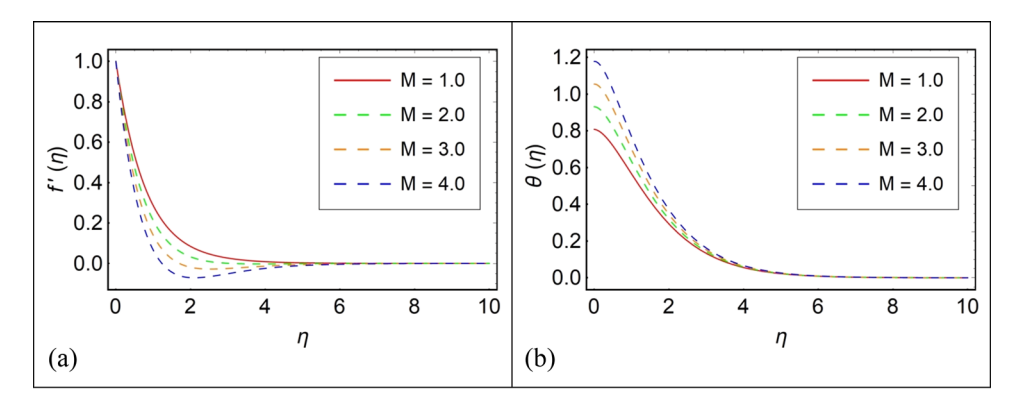


Figure 4: (a) impression of M on $f'(\eta)$ and (b) impression of M on $\theta(\eta)$.

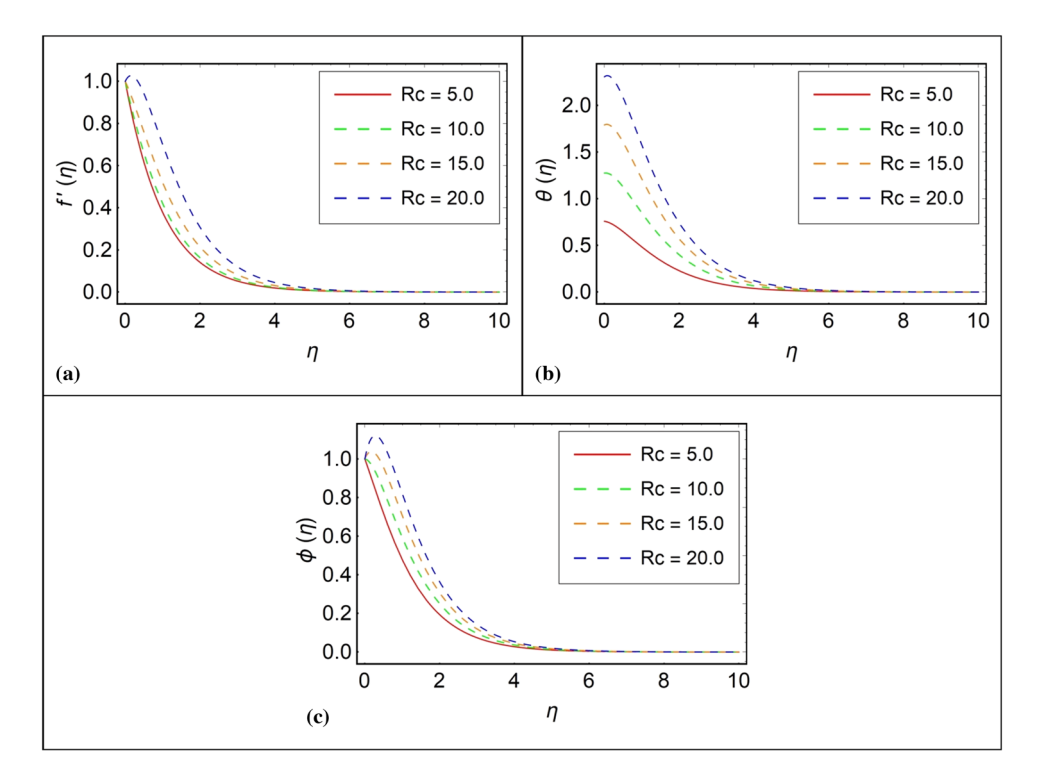


Figure 5: (a) Impression of Rc on $f'(\eta)$, (b) impression of Rc on $\theta(\eta)$, and (c) impression of Rc on $\phi(\eta)$.

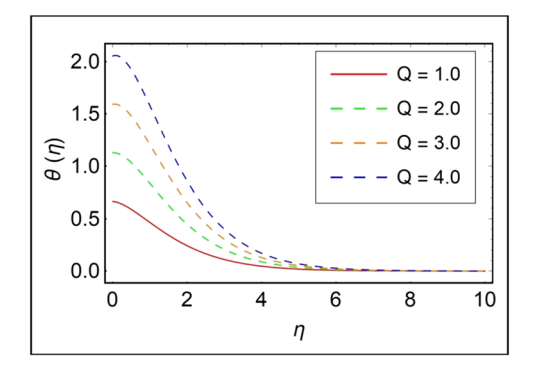


Figure 6: Impression of Q on $\theta(\eta)$.

graphs show that for larger values of Nt, both the thermal and volumetric fraction distributions increase in boundary layer area. This is attributed to the phenomenon that particles near a heated surface generate a thermophoretic force, aiding in the dispersion of particles away from the fluid region. Consequently, this leads to an increase in the thickness of the temperature and volumetric fraction distribution boundary layers. Thus, increasing Nt heightens both $\theta(\eta)$ and $\phi(\eta)$. Figure 8(a) and (b) shows the impact of Nb on $\theta(\eta)$ and $\phi(\eta)$. Upsurge in Nb increases the thermal distribution and reduces the volumetric fraction distribution. The Brownian motion occurs when suspended nanoparticles

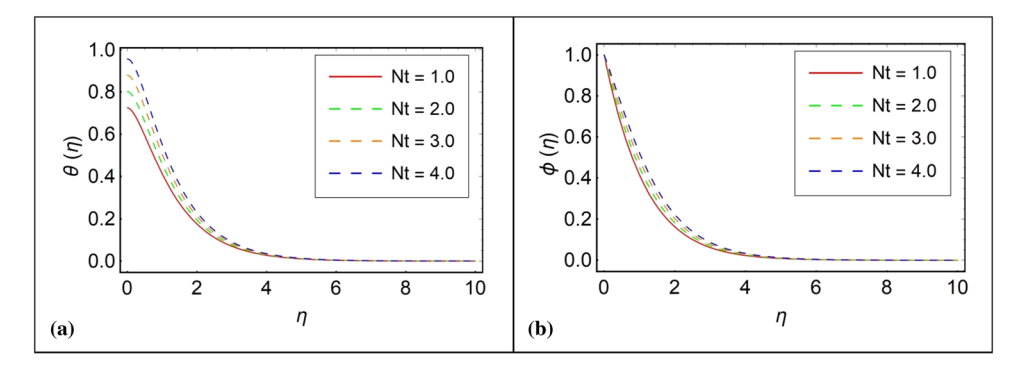


Figure 7: (a) Impression of Nt on $\theta(\eta)$ and (b) impression of Nt on $\phi(\eta)$.

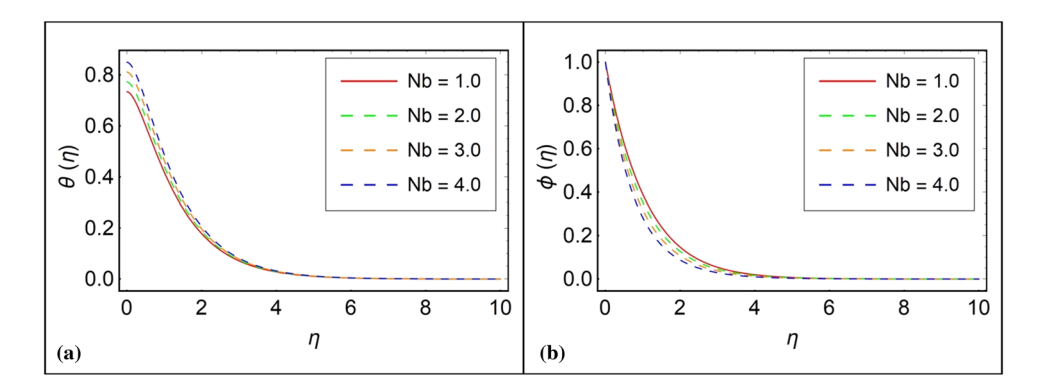


Figure 8: (a) Impression of Nb on $\theta(\eta)$ and (b) impression of Nb on $\phi(\eta)$.

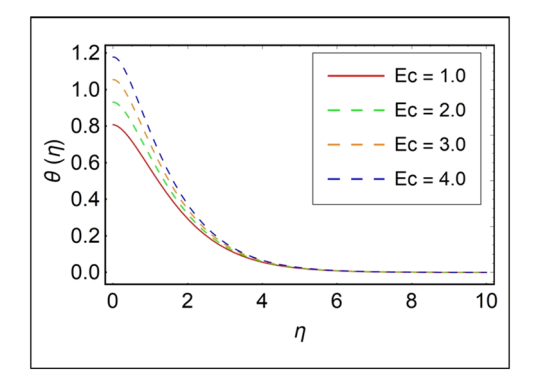


Figure 9: Impression of Ec on $\theta(\eta)$.

move randomly in the base fluid caused by fast-moving molecules or atoms. It should be noted that the Brownian motion is related to nanoparticle size and usually occurs as aggregates or agglomerates. A large particle will have a very weak Brownian motion, and the factor (Nb) will have the smallest value. Boost in Nb increases the boundary layer region, and boosting temperature distribution is depicted in Figure 8(a). Figure 8(b) shows, however, that a higher (Nb) value results in a slower growth in nanoparticle volumetric fraction distribution. Figure 9 illustrates the effects of

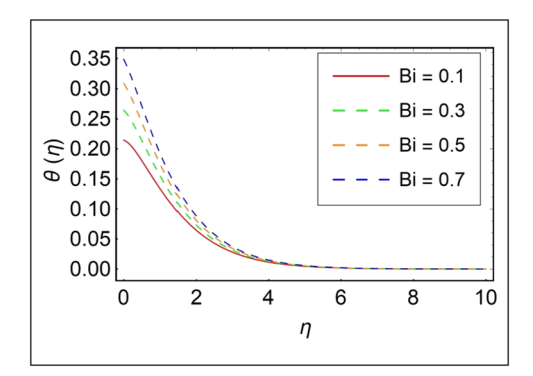


Figure 10: Impression of Bi on $\theta(\eta)$.

the Eckert number (Ec) on $\theta(\eta)$ with a growing behavior of $\theta(\eta)$ with variations in Ec. As Ec grows, frictional heating produces heat in the fluid. The Eckert number is a physical parameter that signifies the ratio of kinetic energy to the specific enthalpy difference between a wall and a fluid. Consequently, as the Eckert number increases, there is a conversion of kinetic energy into internal energy through the work performed against viscous fluid forces. As a result, rising Ec raises the values of $\theta(\eta)$. Figure 10 shows the impact of Biot number (Bi) on $\theta(\eta)$. Based on this figure, it

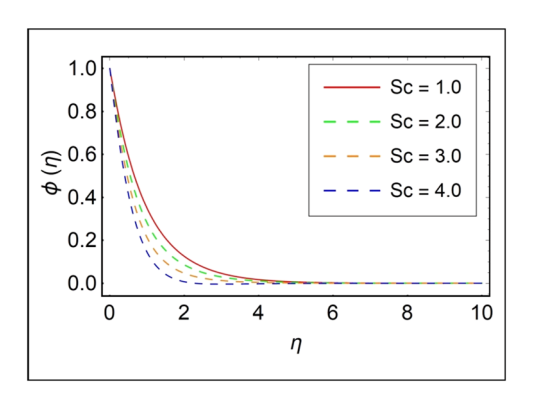


Figure 11: Impression of Sc on $\phi(\eta)$.

can be observed that the temperature distribution increases with higher values of Bi. In fact, higher values of Bi enhance the heat transfer rate at the curved surface of the sheet. This increased rate of heat transfer results in the expansion of the temperature boundary layer thickness and subsequently raises the overall temperature. Consequently, higher values of Bi lead to an increased temperature distribution. Figure 11 displays the effect of the Schmidt number (Sc) on $\phi(\eta)$, where an upsurge is noted in $\phi(\eta)$ for variations in Sc. Actually, mass diffusivity and Schmidt number are inversely proportional to each other. So from here, as Scincreases, the mass diffusivity increases that results in a reduction in $\phi(\eta)$. Table 4 shows the variation in the Nusselt number via variations in M, Ec, Nb, Nt, Bi, and $\chi_1 = \chi_2 = \chi_3$.

Table 4: Nusselt number for different values of M, Ec, Nb, Nt, Bi, and $\chi_1 = \chi_2 = \chi_3$

$\chi_1 = \chi_2 = \chi_3$	M	Ec	Nb	Nt	Bi	$\frac{Nu_s}{\sqrt{Re_s}}$
0.01						0.986684
0.02						1.243256
0.03						1.486474
0.04						1.625784
	0.1					0.486546
	1.2					0.497549
	1.9					0.510753
		0.3				0.609543
		0.6				0.658074
		0.9				0.697544
			0.5			0.508538
			0.7			0.497538
			0.9			0.480746
				0.1		0.696743
				0.5		0.666436
				0.9		0.620753
					0.1	0.597438
					0.3	0.637906
					0.5	0.675274

Table 5: Sherwood number for different values of Nb and Nt

Nb	Nt	$\frac{\mathrm{Sh}_{S}}{\sqrt{\mathrm{Re}_{S}}}$
0.5		0.864753
0.7		0.896447
0.9		0.925789
	0.1	0.596537
	0.5	0.608637
	0.9	0.612483

The increasing $\chi_1 = \chi_2 = \chi_3$ shows the increasing variation in the Nusselt number. The reason is that the higher values $\chi_1 = \chi_2 = \chi_3$ increase the thermal conductivity of the ternary hybrid nanofluid flow, which results in an augmenting variation in the Nusselt number. The higher magnetic factor increases the Nusselt number. The rationale behind this is that a higher magnetic factor diminishes the particle motion, thereby resulting in an increase in temperature and heat transfer rate at the curved surface. Consequently, the Nusselt number rises as the magnetic factor increases. Furthermore, higher values of the Eckert number and thermal Biot number also contribute to an increased Nusselt number. Conversely, the Nusselt number decreases with higher thermophoresis and Brownian motion factors. Similarly, the higher thermophoresis and Brownian motion factors heighten the Sherwood number, as shown in Table 5.

7 Conclusion

A ternary hybrid nanofluid flow with TiO_2 , $CoFe_2O_4$, and MgO nanoparticles over a curved sheet has been examined in this effort. The modeled equations are converted to ODEs using suitable similarity variables. The semi-analytical solution is determined by HAM. The impacts of magnetic field, Joule heating, chemical reaction, and other factors have been discussed on flow profiles and Nusselt, Sherwood numbers using figures and tables. By completing this theoretical analysis, the following concluding points are extracted:

- The velocity distribution exhibits a decreasing trend with respect to the magnetic parameter, while the temperature distribution demonstrates an increasing trend with respect to the magnetic parameter.
- 2) The greater curvature parameter boots the flow, thermal, and volumetric fraction distributions.
- 3) Higher heat source factor, the Eckert and thermal Biot numbers increase the thermal distribution.

- 4) Thermal and volumetric fraction distributions are the growing functions of the thermophoresis factor.
- 5) Thermal distribution has booted up with upsurge in the Brownian factor, while the volumetric fraction distribution panels have retarded with growth in the Brownian factor and the Schmidt number.
- 6) The higher magnetic parameter, Eckert and thermal Biot numbers increase the Nusselt number while reduces with the higher Brownian and thermophoresis factors.
- 7) Higher Brownian and thermophoresis factors heighten the Sherwood number.

Acknowledgments: This research was supported by the Princess Nourah bint Abdulrahman University Researchers Supporting Project number (PNURSP2023R259), Princess Nourah bint Abdulrahman University, Riyadh, Saudi Arabia.

Funding information: This research was supported by the Princess Nourah Bint Abdulrahman University Researchers Supporting Project Number (PNURSP2023R259), Princess Nourah Bint Abdulrahman University, Riyadh, Saudi Arabia.

Author contributions: All authors have accepted responsibility for the entire content of this manuscript and approved its submission.

Conflict of interest: The authors state no conflict of interest.

References

- [1] Choi SUS, Eastman JA. Enhancing thermal conductivity of fluids with nanoparticles. Int. Mech. Eng. Congr. Exhib. San Fr. CA (United States): 1995. p. 12–7. https://digital.library.unt.edu/ark:/67531/ metadc671104/ (accessed October 2, 2021).
- [2] Mourad A, Abderrahmane A, Younis O, Marzouki R, Alazzam A. Numerical simulations of magnetohydrodynamics natural convection and entropy production in a porous annulus bounded by wavy cylinder and Koch snowflake loaded with Cu–Water nanofluid. Micromachines. 2022;13:182.
- [3] Acharya N, Mabood F, Shahzad SA, Badruddin IA. Hydrothermal variations of radiative nanofluid flow by the influence of nanoparticles diameter and nanolayer. Int Commun Heat Mass Transf. 2022;130:105781. doi: 10.1016/J.ICHEATMASSTRANSFER.2021.105781.
- [4] Shahid A, Bhatti MM, Ellahi R, Mekheimer KS. Numerical experiment to examine activation energy and bi-convection Carreau nanofluid flow on an upper paraboloid porous surface: Application in solar energy. Sustain Energy Technol Assessments. 2022;52:102029.
- [5] Bhatti MM, Arain MB, Zeeshan A, Ellahi R, Doranehgard MH. Swimming of Gyrotactic Microorganism in MHD Williamson nanofluid flow between rotating circular plates embedded in porous

- medium: Application of thermal energy storage. J Energy Storage. 2022;45:103511.
- [6] Wijayanta AT. Numerical solution strategy for natural convection problems in a triangular cavity using a direct meshless local Petrov-Galerkin method combined with an implicit artificial-compressibility model. Eng Anal Bound Elem. 2021;126:13–29.
- [7] Wijayanta AT. A localized meshless approach using radial basis functions for conjugate heat transfer problems in a heat exchanger. Int J Refrig. 2020;110:38–46.
- [8] Makarim DA, Suami A, Wijayanta AT, Kobayashi N, Itaya Y. Marangoni convection within thermosolute and absorptive aqueous LiBr solution. Int J Heat Mass Transf. 2022;188:122621.
- [9] Kumar RSV, Dhananjaya PG, Kumar RN, Gowda RJP, Prasannakumara BC. Modeling and theoretical investigation on Casson nanofluid flow over a curved stretching surface with the influence of magnetic field and chemical reaction. Int J Comput Methods Eng Sci Mech. 2022;23:12–9.
- [10] Zhang L, Bhatti MM, Michaelides MM, Marin M, Ellahi R. Hybrid nanofluid flow towards an elastic surface with tantalum and nickel nanoparticles, under the influence of an induced magnetic field. Eur Phys J Spec Top. 2022;231:521–33.
- [11] Khan A, Saeed A, Tassaddiq A, Gul T, Mukhtar S, Kumam P, et al. Bio-convective micropolar nanofluid flow over thin moving needle subject to Arrhenius activation energy, viscous dissipation and binary chemical reaction. Case Stud. Therm Eng. 2021;25:100989.
- [12] Chu Y, Bashir S, Ramzan M, Malik MY. Model-based comparative study of magnetohydrodynamics unsteady hybrid nanofluid flow between two infinite parallel plates with particle shape effects. Math Methods Appl Sci. 2023 Jul 15;46(10):11568–82.
- [13] Ojjela O. Numerical investigation of heat transport in Alumina–Silica hybrid nanofluid flow with modeling and simulation. Math Comput Simul. 2022;193:100–22.
- [14] Gumber P, Yaseen M, Rawat SK, Kumar M. Heat transfer in micropolar hybrid nanofluid flow past a vertical plate in the presence of thermal radiation and suction/injection effects. Partial Differ Equations Appl Math. 2022;5:100240.
- [15] Slimani R, Aissa A, Oudina FM, Khan U, Sahnoun M, Chamkha AJ, et al. Natural convection analysis flow of Al2O3-Cu/water hybrid nanofluid in a porous conical enclosure subjected to the magnetic field. Eur Phys J Appl Phys. 2020;92:10904. doi: 10.1051/EPJAP/2020200260.
- [16] Arif M, Persio LD, Kumam P, Watthayu W, Akgül A. Heat transfer analysis of fractional model of couple stress Casson tri-hybrid nanofluid using dissimilar shape nanoparticles in blood with biomedical applications. Sci Rep. 2023;13:4596.
- [17] Shahzad F, Jamshed W, Eid MR, Ibrahim RW, Aslam F, Isa SSPM, et al. The effect of pressure gradient on MHD flow of a tri-hybrid Newtonian nanofluid in a circular channel. J Magn Magn Mater. 2023:568:170320.
- [18] Sudharani M, Prakasha DG, Kumar KG, Chamkha AJ. Computational assessment of hybrid and tri hybrid nanofluid influenced by slip flow and linear radiation. Eur Phys J Plus. 2023;138:257.
- [19] Guedri K, Khan A, Sene N, Raizah Z, Saeed A, Galal AM. Thermal flow for radiative ternary hybrid nanofluid over nonlinear stretching sheet subject to Darcy–Forchheimer phenomenon. Math. Probl. Eng. 2022;2022:3429439.
- [20] Shevchuk IV. An improved asymptotic expansion method for fluid flow and convective heat transfer in cone-and-disk geometries with rotating cone. Phys Fluids. 2023;35:43603.
- [21] Olayemi OA, Khaled AF, Temitope OJ, Victor OO, Odetunde CB, Adegun IK. Parametric study of natural convection heat transfer

- from an inclined rectangular cylinder embedded in a square enclosure. Aust | Mech Eng. 2023;21:668–81.
- [22] Manna NK, Biswas N, Mandal DK, Sarkar UK, Öztop HF, Hamdeh NH. Impacts of heater-cooler position and Lorentz force on heat transfer and entropy generation of hybrid nanofluid convection in quarter-circular cavity. Int J Numer Methods Heat Fluid Flow. 2023;33:1249–86.
- [23] Wang SR, Wang CA. Numerical simulation of convective heat transfer in packed bed using open-source computational fluid dynamics. Powder Technol. 2023;422:118452.
- [24] Shi L, Zhu X, Du Z. Study on convective heat transfer characteristics of inclined jet impinging cylindrical target surface in the confined space. Appl Therm Eng. 2023;218:119316.
- [25] Abbas A, Jeelani MB, Alharthi NH. Darcy–Forchheimer relation influence on MHD dissipative third-grade fluid flow and heat transfer in porous medium with joule heating effects: A numerical approach. Processes. 2022;10:906.
- [26] Naseem T, Fatima U, Munir M, Shahzad A, Kausar N, Nisar KS, et al. Joule heating and viscous dissipation effects in hydromagnetized boundary layer flow with variable temperature, Case Stud. Therm Eng. 2022;35:102083.
- [27] Rasheed HU, Islam S, Zeeshan, Abbas T, Khan J. Analytical treatment of MHD flow and chemically reactive Casson fluid with Joule heating and variable viscosity effect. Waves Random Complex Media. 2022;1–17. doi: 10.1080/17455030.2022.2042622.
- [28] Mahdy AMS, Babatin MM, Khader MM. Numerical treatment for processing the effect of convective thermal condition and Joule heating on Casson fluid flow past a stretching sheet. Int J Mod Phys C. 2022;33:2250108.
- [29] Waqas H, Sadiq MA, Bahaidarah HMS. Gyrotactic bioconvection stratified flow of magnetized micropolar nanoliquid configured by stretchable radiating surface with Joule heating and viscous dissipation. Int Commun Heat Mass Transf. 2022;138:106229.
- [30] Mahanthesh B, Reddy CS, Srikantha S, Lorenzini G. Entropy generation analysis of radiative heat transfer in Williamson fluid flowing in a microchannel with nonlinear mixed convection and Joule heating. Proc Inst Mech Eng Part E J Process Mech Eng. 2022;09544089221074846. doi: 10.1177/09544089221074846.
- [31] Gangadhar K, Lakshmi KB, Kannan T, Chamkha AJ. Bioconvective magnetized oldroyd-B nanofluid flow in the presence of Joule heating with gyrotactic microorganisms. Waves Random Complex Media. 2022;1–21. doi: 10.1080/17455030.2022.2050441.
- [32] Mishra A, Upreti H. A comparative study of Ag-MgO/water and Fe3O4-CoFe2O4/EG-water hybrid nanofluid flow over a curved surface with chemical reaction using Buongiorno model. Partial Differ Equations Appl Math. 2022;5:100322.
- [33] Maity S, Kundu PK. Magnetically driven chemically reactive Casson nanofluid flow over curved surface with thermal radiation. Heat Transf. 2022;51:4882–905.
- [34] Khan U, Zaib A, Ishak A, Bakar AS, Animasaun IL, Yook SJ. Insights into the dynamics of blood conveying gold nanoparticles on a curved surface when suction, thermal radiation, and Lorentz force are significant: The case of Non-Newtonian Williamson fluid. Math Comput Simul. 2022;193:250–68.
- [35] Sun Z, Shi Z, Li Z, Geng X, Sun Q, Chen S, et al. Experimental investigation of flow control of a curved-surface jet hypersonic flow. Phys Fluids. 2022;34:66107.
- [36] Fuzhang W, Anwar MI, Ali M, El-Shafay AS, Abbas N, Ali R. Inspections of unsteady micropolar nanofluid model over exponentially stretching curved surface with chemical reaction. Waves

- Random Complex Media. 2022;1–22. doi: 10.1080/17455030.2021. 2025280.
- [37] Nadeem S, Abbas N, Malik MY. Inspection of hybrid based nanofluid flow over a curved surface. Comput Methods Programs Biomed. 2020;189:105193. doi: 10.1016/j.cmpb.2019.105193.
- [38] Sarada K, Gamaoun F, Abdulrahman A, Paramesh SO, Kumar R, Prasanna GD, et al. Impact of exponential form of internal heat generation on water-based ternary hybrid nanofluid flow by capitalizing non-Fourier heat flux model. Case Stud Therm Eng. 2022;38:102332.
- [39] Dawar A, Islam S, Shah Z, Mahmuod SR. A passive control of Casson hybrid nanofluid flow over a curved surface with alumina and copper nanomaterials: A study on sodium alginate-based fluid. I Mol Lig. 2023;382:122018.
- [40] Sun X, Animasaun IL, Swain K, Shah NA, Wakif A, Olanrewaju PO. Significance of nanoparticle radius, inter-particle spacing, inclined magnetic field, and space-dependent internal heating: The case of chemically reactive water conveying copper nanoparticles. ZAMM-J Appl Math Mech Für Angew Math Und Mech. 2022;102:e202100094.
- [41] Dawar A, Wakif A, Saeed A, Shah Z, Muhammad T, Kumam P. Significance of Lorentz forces on Jeffrey nanofluid flows over a convectively heated flat surface featured by multiple velocity slips and dual stretching constraint: a homotopy analysis approach. J Comput Des Eng. 2022;9:564–82.
- [42] Souayeh B, Ramesh K. Numerical scrutinization of ternary nanofluid flow over an exponentially stretching sheet with gyrotactic microorganisms. Mathematics. 2023;11(4):981.
- [43] Priyadharshini P, Archana MV, Shah NA, Alshehri MH. Ternary hybrid nanofluid flow emerging on a symmetrically stretching sheet optimization with machine learning prediction scheme. Symmetry. 2023;15:1225.
- [44] Wang F, Nazir U, Sohail M, El-Zahar ER, Park C, Thounthong P. A Galerkin strategy for tri-hybridized mixture in ethylene glycol comprising variable diffusion and thermal conductivity using non-Fourier's theory. Nanotechnol Rev. 2022;11:834–45.
- [45] Acharya N, Maity S, Kundu PK. Framing the hydrothermal features of magnetized TiO2–CoFe2O4 water-based steady hybrid nanofluid flow over a radiative revolving disk. Multidiscip. Model Mater Struct. 2020;16:765–90. doi: 10.1108/MMMS-08-2019-0151/ FULL/XMI.
- [46] Mishra A, Pandey AK, Kumar M. Thermal performance of Ag–water nanofluid flow over a curved surface due to chemical reaction using Buongiorno's model. Heat Transf. 2021;50:257–78.
- [47] Abbas Z, Naveed M, Sajid M. Hydromagnetic slip flow of nanofluid over a curved stretching surface with heat generation and thermal radiation. J Mol Liq. 2016;215:756–62.
- [48] Algehyne EA, Wakif A, Rasool G, Saeed A, Ghouli Z. Significance of Darcy-Forchheimer and Lorentz forces on radiative aluminawater nanofluid flows over a slippery curved geometry under multiple convective constraints: a renovated Buongiorno's model with validated thermophysical correlations. Waves Random Complex Media. 2022;1–30. doi: 10.1080/17455030.2022. 2074570.
- [49] Roşca NC, Pop I. Unsteady boundary layer flow over a permeable curved stretching/shrinking surface. Eur J Mech. 2015;51:61–7.
- [50] Afridi MI, Qasim M, Wakif A, Hussanan A. Second law analysis of dissipative nanofluid flow over a curved surface in the presence of Lorentz Force: Utilization of the Chebyshev–Gauss–Lobatto

- spectral method. Nanomater. 2019;9:195. doi: 10.3390/ NANO9020195.
- [51] Abbas Z, Naveed M, Sajid M. Heat transfer analysis for stretching flow over a curved surface with magnetic field. J Eng Thermophys. 2013;22:337-45.
- [52] Ahmad S, Nadeem S, Muhammad N. Boundary layer flow over a curved surface imbedded in porous medium. Commun Theor Phys. 2019;71:344.
- [53] Dey D, Makinde OD, Chutia B. Hydromagnetic flow of dusty fluid with heat and mass transfer past a stretching curved surface in a porous medium. Lat Am Appl Res. 2022;52:201-6.
- [54] Khan WA, Pop I. Boundary-layer flow of a nanofluid past a stretching sheet. Int J Heat Mass Transf. 2010;53:2477-83.
- [55] Wang CY. Free convection on a vertical stretching surface. ZAMM-J Appl Math Mech Für Angew Math Und Mech. 1989;69:418-20.

- [56] Gorla RS, Sidawi I. Free convection on a vertical stretching surface with suction and blowing. Appl Sci Res. 1994;52:247-57.
- [57] Devi SU, Devi SPA. Heat transfer enhancement of cu- \$ al_ {2} o_ {3} \$/water hybrid nanofluid flow over a stretching sheet. J Niger Math Soc. 2017;36:419-33.
- [58] Grubka LG, Bobba KM. Heat transfer characteristics of a continuous stretching surface with variable temperature. J Heat Transfer. 1985;107:248-50.
- [59] Gowda RJP, Al-Mubaddel FS, Kumar RN, Prasannakumara BC, Issakhov A, Rahimi-Gorji A, et al. Computational modelling of nanofluid flow over a curved stretching sheet using Koo-Kleinstreuer and Li (KKL) correlation and modified Fourier heat flux model. Chaos Solit Fractals. 2021:145:110774.